

Spin-Orbit Proximity Effect in Graphene

A. Avsar^{1,2}, J. Y. Tan^{1,2}, J. Balakrishnan^{1,2}, G. K. W. Koon^{1,2,3}, J. Lahiri^{1,2}, A. Carvalho^{1,2}, A. S. Rodin⁴, T. Taychatanapat^{1,2}, E. C. T. O'Farrell^{1,2}, G. Eda^{1,2}, A. H. Castro Neto^{1,2} & B. Özyilmaz^{1,2,3*}

¹Department of Physics, National University of Singapore, 117542, Singapore

²Graphene Research Center, National University of Singapore, 117542, Singapore

³NanoCore, National University of Singapore, 117576, Singapore

⁴Department of Physics, Boston University, Boston, MA, 02215, USA

*email: barbaros@nus.edu.sg

The development of a spintronics device relies on efficient generation of spin polarized currents and their electric field controlled manipulation. While observation of exceptionally long spin relaxation lengths make graphene an intriguing material for spintronics studies, modulation of spin currents by gate field is almost impossible due to negligibly small intrinsic spin orbit coupling (SOC) of graphene. In this work, we create an artificial interface between monolayer graphene and few-layers semiconducting tungsten disulfide (WS₂). We show that in such devices graphene acquires a SOC as high as 17meV, three orders of magnitude higher than its intrinsic value, without modifying any of the structural properties of the graphene. Such proximity SOC leads to the spin Hall effect even at room temperature and opens the doors for spin FETs. We show that intrinsic defects in WS₂ play an important role in this proximity effect and that graphene can act as a probe to detect defects in semiconducting surfaces.

Graphene is a promising material for both fundamental spin based transport phenomena and low power consuming spin based device applications¹⁻². Among the first predictions for graphene was the topological insulator with spin polarized edge states³. Furthermore, room temperature (RT) ballistic charge transport⁴ and gate-tunability make graphene an ideal material for spin field effect transistors (FETs)⁵. However, graphene's extremely weak intrinsic spin-orbit coupling (SOC)⁶ makes the experimental observation of these phenomena very challenging. Previous studies have shown that the weak hydrogenation of graphene can significantly enhance the SOC⁷⁻⁸. However, chemical functionalization introduces disorder and severely limits charge mobility and hence, the spin relaxation length⁸⁻⁹. Equally important, the hybridization between hydrogen and carbon induces a Rashba type SOC by introducing sp₃ defects thereby breaking the inversion symmetry of the lattice¹⁰. The decoration of the graphene surface with heavy metal

adatoms such as gold (Au), indium (In) or thallium (Tl) has also been proposed to increase the spin orbit coupling¹¹⁻¹². However, also this approach introduces disorder and hence, equally limits both charge and spin transport properties¹³.

These challenges have recently brought to light other 2D crystals such as transition metal dichalcogenides (TMDC). TMDCs have band gaps in a technologically attractive energy range (~1-2 eV) and orders of magnitude higher SOC than graphene¹⁴. This, combined with spin split bands makes them an almost ideal material for spintronics. However, the presence of unavoidable defects in TMDCs typically limits their electron mobilities to $\mu \sim 100 \text{ cm}^2/\text{V.s}^{15}$. Hence, we expect a spin relaxation length even lower than in weakly hydrogenated graphene. In this work, we show that by utilizing the proximity effect between graphene and TMDCs one can keep the extraordinary high mobilities of crystalline graphene and at the same time enhance its SOC to allow electric field controllable spin currents at room temperature.

Since graphene and WS_2 have comparable workfunctions (~4.6 eV and ~ 4.7 eV, respectively)¹⁶⁻¹⁸, the charge neutrality point of graphene on WS_2 is expected to be located approximately in the middle of the energy gap of WS_2 . Therefore, naively, one would expect WS_2 to act just as another inert substrate such as SiO_2 or BN. Remarkably, the presence of intrinsic disorder in WS_2 creates electronic midgap states which hybridize with the electronic states of graphene. Because of the finite thickness of the WS_2 (~ 10nm) substrate, the number of these defects is large. Thus, above a threshold back gate voltage (V_{TH}) they act as a sink for electronic charges, resulting in a gate bias (V_{BG}) **independent** conductivity. For $V_{\text{BG}} < V_{\text{TH}}$, our devices have electronic mobilities as high as $50.000 \text{ cm}^2/\text{V.s}^{19}$, comparable to what has been reported on BN substrates²⁰ with no signature of SOC enhancement. In contrast, for $V_{\text{BG}} > V_{\text{TH}}$, we found a giant enhancement of SOC (~17meV). The combination of high charge mobility and

large proximity induced SOC results in a gate tunable spin Hall effect (SHE) even at RT, a crucial ingredient in realizing spintronics paradigms such as the spin FET⁵ and potentially even the quantum spin Hall insulator³.

The fabrication of graphene/WS₂ heterostructure devices starts with the standard dry transfer method⁴ of single layer graphene (SLG) onto atomically flat few layers of WS₂ (Fig. 1A). Subsequently, e-beam lithography is used to form electrodes and pattern graphene into a Hall bar. Typical channel lengths and widths are $l = 3\mu\text{m}$ and $w = 1\mu\text{m}$ respectively. A pair of electrodes is also created directly on WS₂. An optical image of a typical final device is shown in Fig. 1B. Experiments were carried out in two different measurement configurations. In the conventional local four terminal measurement configuration (Hall bar), current I_{16} flows between contact 1 and contact 6 and a local voltage drop is measured between contact 2 and contact 4. In the non-local measurement configuration (H bar), the current I_{23} flows between the pair of contact 2 and contact 3 and a non-local voltage V_{45} is recorded across the neighboring pair of contact 4 and contact 5 (Fig. 1C). All measurements were performed with standard ac lock-in technique at low frequencies in vacuum as a function of magnetic (B), back gate voltage (V_{BG}) at both room temperature (RT) and liquid Helium temperatures. In total, we have characterized 10 Graphene/WS₂ devices. Here we discuss 2 representative devices and unless otherwise stated, the results shown are from device B.

Fig. 2A shows the local conductivity σ of graphene on a WS₂ substrate as a function of V_{BG} at $T = 1.5\text{ K}$ ($\mu_{\text{h}} \approx 18,000\text{ cm}^2/\text{V.s.}$). While on the hole side σ is linear in V_{BG} , on the electron side σ saturates above a threshold voltage $V_{\text{TH}} \geq 15\text{V}$. A similar behavior has been observed in all graphene on WS₂ devices and is absent e.g. in graphene on BN devices. We also performed two terminal I-V measurements directly across WS₂ alone. To minimize any shunting of the

current through the WS₂, we use Cr/Au contacts (see SI). In such measurements, only an insulating response over the same V_{BG} range is observed¹⁹. Next, we discuss perpendicular magnetic field (B_⊥) dependent measurements as shown in Fig. 2B-C. From Hall effect measurements at low fields, we see that the origin of the conductance saturation on the electron side is due to the saturation of the charge density at $\sim 7 \times 10^{11} \text{ cm}^{-2}$ (Inset-Fig. 2C). The electron mobility above the saturation region is estimated to be $\mu_e \approx 24,750 \text{ cm}^2/\text{V.s}$. In high B_⊥ fields, this surprising result even alters the well known Landau level (LL) fan diagram of graphene. This is clearly seen in the fan diagram where the longitudinal resistance, R_{XX}, is recorded on a color plot as a function of both V_{BG} and the perpendicularly applied B_⊥ (Fig. 2B). For example, at B_⊥ = 4.5T, R_{XX} vs V_{BG} shows the regular integer quantum hall effect on the hole side with filling factor $\nu=2, 6, 10, 14, 18, 22$. However, on the electron side only the quantization for the first two LLs is observed. Since the LLs in graphene are not equally spaced in energy, it is possible to lock the graphene resistance even at the first LL for $|B_{\perp}| > 10\text{T}$ (Fig. 2C), making such graphene/WS₂ heterostructure potentially a suitable device for quantum resistance metrology²¹.

We now turn our attention to non-local transport measurements. This measurement technique is a powerful tool to detect spin dependent transport phenomena that otherwise escape notice. Recently, this configuration has been for example used to detect Zeeman interaction induced spin currents in graphene in the presence of an externally applied perpendicular magnetic field²²⁻²³. Balakrishnan *et al*, also implemented this geometry to demonstrate an enhancement of SOC in hydrogenated graphene by measuring spin precession in an in-plane magnetic field¹⁰. We first discuss the RT non-local measurement of a graphene on SiO₂ device of comparable mobility ($\mu \approx 13,000 \text{ cm}^2/\text{V.s}$) (Fig. 3A). For such devices the non-local resistance

is *symmetric* around the Dirac peak and its magnitude over the entire back gate bias range can be fully accounted for by an Ohmic leakage contribution²⁴, $\sim \rho e^{-\pi L/w}$ (dashed dotted fit to the data). In contrast, graphene on WS₂ substrates (Devices B and C, Fig. 3B and C) shows a non-local signal which cannot be accounted for by an Ohmic contribution neither quantitatively nor qualitatively. First, the magnitude of the observed non-local signal is almost an order of magnitude larger than in graphene on SiO₂ samples. More importantly, we observe a strong electron-hole *asymmetry* in non-local resistance, which is completely absent in both graphene on SiO₂ and even in graphene on BN substrates (not shown). For instance, device B and device C have a non-local signal difference ΔR between the hole side and electron side of $\Delta R \sim 8\Omega$ and $\Delta R \sim 20\Omega$, respectively. We find that there is a sample to sample variation of the non-local signal¹⁹ most likely due to a variation in the amount of the disorder in each sample. However, the electron-hole asymmetry in the non-local signal is observed in all our graphene-WS₂ devices. Equally important, the onset of the asymmetry coincides with V_{TH} at which the local conductivity saturates. Note that this asymmetry does rule out thermal effects as discussed in ref.23 as the dominant effect.

To determine the origin of the non-local signal, we applied a magnetic field B_{\parallel} in the plane of the device parallel to the current flow direction. Such Hanle spin precession measurements for device B as a function of V_{BG} are summarized in Fig. 4D. Also here we see a clear electron-hole asymmetry. The critical gate voltage at which the field dependence of the non-local signal changes dramatically coincides again with V_{TH} at which the conductance saturation is observed. For all $V_{BG} < V_{TH}$, the non-local signal is magnetic field *independent*. Two representative R_{NL} vs B_{\parallel} traces at $V_{BG} = -37$ V and $V_{BG} = 2$ V (DP) are shown in Fig. 3D. On the other hand For all $V_{BG} > V_{TH}$, the nonlocal signal shows a maximum at zero magnetic

field and decreases with increasing $|B_{\parallel}|$ with the onset of an oscillatory behavior clearly visible for $|B_{\parallel}| > 8$ T. Remarkably, the maximum observed change of the non-local signal $\Delta R = 8\Omega$ as a function of field is comparable to the difference observed in the non-local signal ΔR as a function of V_{BG} (Fig. 3B). It is important to note that in this measurement configuration only a spin current can give rise to a magnetic field dependent signal²⁵. Thus, the observation of oscillatory magnetic field dependent signal directly proves the spin origin of the non-local signal. We are now ready to extract the spin transport parameters of our devices. For this we fit the field dependence of the nonlocal signal using the following equation²⁴:

$$R_{NL} = \frac{1}{2} \gamma^2 w \rho \operatorname{Re} \left[\left(\sqrt{1 + i\omega_B \tau_s} / \lambda_s \right) e^{-(\sqrt{1 + i\omega_B \tau_s} / \lambda_s) L} \right]$$

where γ is the spin Hall coefficient, w the width of the channel, ρ is the resistivity of the channel, ω_B is the Larmor frequency, τ_s is the spin relaxation time, and λ_s is the spin relaxation length. We obtain $\lambda_s = 2 \mu\text{m}$, τ_s of 5 ps. The strongly reduced τ_s , when compared with τ_s of even hydrogenated spin valves (9) ($\sim 0.7\text{ns}$) is direct consequence of the colossal enhancement of SOC.

We finally calculate the proximity SOC strength Δ_{SO} . Since the dominant dephasing mechanism in SLG is Elliott-Yafet type (1,26) we have $\Delta_{SO} = \varepsilon_F \sqrt{(\tau_P / \tau_S)}$ (27) where ε_F is the Fermi energy and τ_P is the momentum relaxation time, $\tau_P = h\sigma / 2e^2 v_F \sqrt{(\pi n)}$. Thus, we obtain a proximity SOC of 17.6 meV which is even higher than that achieved by hydrogenating graphene⁸. With this, we identify the SHE and inverse SHE as the origin of the observed non-local signal. The latter is only possible because of the three order of magnitude enhancement of the intrinsic SOC graphene when in proximity with WS_2 . Low field magneto resistance measurements provided further evidence for a strong enhancement of the spin-orbit coupling for $V_{BG} > V_{TH}$. Here, we see at the same threshold voltage a transition from positive to negative MR.

This change from weak localization to weak-antilocalization behavior provides independent evidence for the proximity effect induced SOC (See S.I.).

Next we discuss the origin of the proximity effect in more detail. Recently single sulphur vacancies have been observed in MoS₂ flakes by using an atomic resolution direct imaging technique²⁸⁻²⁹. Similar structural defects are also expected for WS₂ crystals. For this purpose, we characterized our CVD grown WS₂ crystals with X-ray photoelectron spectroscopy (XPS). Fig. 4A shows the XPS spectra of W_{4f} and S_{2p} from where we estimate a large concentration of sulphur vacancies of the order of 10¹³cm⁻² (See S.I. for discussion). This result shows that there are localized states in the gap of WS₂, originating from sulphur vacancies. As a next step, we performed ab initio fully relativistic density functional theory (DFT) calculations to discuss the relevance of these states on the observed phenomena. Our calculations for the band structure of the graphene/WS₂ interface show that the Dirac point of graphene is within the WS₂ band gap (Fig. 4B). The band structure of the interface is nearly a superposition of the band structures of the two moieties. The lowest conduction band of WS₂ is practically unchanged by the presence of graphene, and its position relative to the Fermi level differ less than 0.1eV from those obtained by the alignment of the vacuum level for the two independent systems. Note that the proximity of WS₂ without vacancies does not induce any significant SOC. A sulphur vacancy (V_S) on the other hand introduces a double unoccupied state in the top half of the band gap of bulk WS₂ (Fig. 4C), as close as ~ 0.1eV to the Fermi level of graphene. In fact, using $\epsilon_f = \hbar v_f \sqrt{\pi n}$ where v_f is the Fermi velocity (0.9x10⁶ m/s) and n is the carrier concentration (7x10¹¹ cm⁻²) at V_{TH} we obtain $\epsilon_f \sim 0.09$ eV at V_{TH} in good agreement with our theoretical estimate. The mid gap states originate on the vacancy dangling bonds and are localized on W. They have an unusually large spin splitting of about $\Delta E_{SO} \sim 0.2$ eV to which we assign the origin of the

proximity SOC observed. The graphene electrons move from graphene to the vacancy states in WS₂ by quantum tunneling. This tunneling relies on the proximity of the wavefunction of the vacancy states to the graphene, which is characterized by hybridization energy V_H . From second order perturbation theory ($\Delta E_{SO} \approx V_H^2/\Delta_{SO}$), the hybridization energy is estimated to be 0.059 eV.

In conclusion, we have demonstrated that graphene is very sensitive to the defects in the underlying WS₂ substrate. These structural defects enhance the weak SOC of graphene while preserving the extraordinary electronic properties. Since all TMDCs have similar structures and properties, this proximity effect is expected to be present in a wide range of different crystals. Our results open a new avenue for the realization of many exotic phenomena such as the quantum SHE.

References

1. A. Avsar *et al.*, *Nano Lett.* **11**, 23632368 (2011).
2. T. Maassen *et al.*, *Nano Lett.* **12**, 1498-1502 (2012).
3. C. L. Kane, E. J. Mele, *Phys. Rev. Lett.* **95**, 226801 (2005).
4. A. S. Mayorov *et al.*, *Nano Lett.* **11**, 2396-2399 (2011).
5. J. Schliemann, J. C. Egues, and D. Loss, *Phys. Rev. Lett.*, **90**, 146801 (2003).
6. S. Konschuh, M. Gmitra, J. Fabian, *Phys. Rev. B* **82**, 245412 (2010).
7. A. H. Castro Neto, F. Guinea, *Phys. Rev. Lett.* **103**, 026804 (2009).
8. J. Balakrishnan, *et al. Nature Phys.* **9**, 284-287 (2013).
9. M. Wojtaszek, I. J. Vera-Marun, T. Maassen, B. J. van Wees, *Phys. Rev. B: Rap. Comm.* **87**, 081402(R) (2013).
10. M. Gmitra, D. Kochan, J. Fabian, Preprint at <http://arxiv.org/abs/1303.2806> (2013).
11. W. Conan, H. Jun, A. Jason, F. Marcel, W. Ruqian, *Phys. Rev. X* **1**, 021001 (2011).
12. D. W. Ma, Z. Y. Z. Q. Li, Yang, *Carbon* **50**, 297 (2012).
13. K. Pi, *et al.*, *Phys. Rev. Lett.* **104**, 187201 (2010).
14. Q. H. Wang, K. Kalantar-Zadeh, A. Kis, J. N. Coleman, M. S. Strano, *Nature Nanotech.* **7**, 699-712 (2012).
15. B. Radisavljevic, A. Radenovic, J. Brivio, V. Giacometti, A. Kis, *Nature Nanotechnol.* **6**, 147-150 (2011).
16. Y. J. Yu, *et al.*, *Nano Lett.* **9**, 3430-3434 (2009).
17. C. Gong, *et al.*, *Applied Phys. Lett.* **103**, 053513 (2013).
18. L. Britnell, *et al.*, *Science* **340**, 1311-1314 (2013).
19. See supporting material on *Science Online*.
20. C. R. Dean, *et al.*, *Nature Nanotechnol.* **5**, 722-726 (2010).

21. T. J. B. M. Janssen, A. Tzalenchuk, S. Lara-Avila, S. Kubatkin, V. I. Fal'ko, *Rep. Prog. Phys.* **76**, 104501 (2013).
22. D. A. Abanin, *et al.*, *Science*, **332**, 328-330 (2011).
23. J. Renard, M. Studer, A. J. Folk, Reprint at <http://arxiv.org/abs/1309.7016> (2013).
24. D. A. Abanin, A. V. Shytov, L. S. Levitov, B. I. Halperin, *Phys. Rev. B* **79**, 035304 (2009).
25. F. J. Jedema, H. B. Heersche, A. T. Filip, J. J. A. Baselmans, B. J. van Wees, *Nature* **416**, 713-716 (2002).
26. C. Józsa, *et al.*, *Phys. Rev. B: Rap. Comm.* **80**, 241403(R) (2005).
27. H. Ochoa, A. H. Castro Neto, Guinea, *Phys. Rev. Lett.* **108**, 206808 (2012).
28. F. Zhou, W. *et al.*, *Nano Lett.* **13**, 2615-2622 (2013).
29. H. Qiu *et al.*, *Nature Comm.*, **4**, 2642 (2013).
30. P. C. Yen *et al.*, *J. Phys.: Condens. Matter*, **16**, 2171 (2004).

Acknowledgments: We thank A. Hamilton and R. Ribeiro for their help and useful discussions. This work was supported by the Singapore National Research Foundation Fellowship award (RF2008-07-R-144-000-245-281), the NRF-CRP award 'Novel 2D materials with tailored properties: beyond graphene' (R-144-000-295-281) and the Singapore Millennium Foundation-NUS Research Horizons award (R-144-001-271-592; R-144-001-271-646).

Author Contributions

B.Ö. and A.H.C.N. devised and supervised the project. A.A. and B.Ö. designed the experiments. A.A. and J.Y.T. did the device fabrication. A.A, J.B, G.K.W.K., T.T, and E.C.T.O carried out the transport measurements. A.H.C.N., A.C. and A.S.R. developed the theoretical aspects of this work. E.G. and J.L grew WS₂ crystals and performed XPS measurements. A.A., A.C., A.H.C.N.

and B.Ö. co-wrote the manuscript. All authors discussed the results and commented on the manuscript.

Additional information

Supplementary information is available in the online version of the paper. Reprints and permissions information is available online at www.nature.com/reprints. Correspondence and requests for materials should be addressed to B. Ö.

Competing financial interests:

The authors declare no competing financial interests.

Figure Captions:

Fig. 1. Device Characterization: (A) Schematics representation of a multilayer WS₂/Graphene heterostructure device. The highest unoccupied state of the sulphur vacancy is depicted in yellow, highlighting on the W atoms closest to the vacancy. W, S and C atoms are represented by dark gray, orange and light gray spheres, respectively. (B) Optical micrograph of a completed device with multiple Hall bar junctions on G/ WS₂ heterostructure and a two terminal device on WS₂. The scale bar is 2µm. (C) Schematics for the local and non-local measurement configurations.

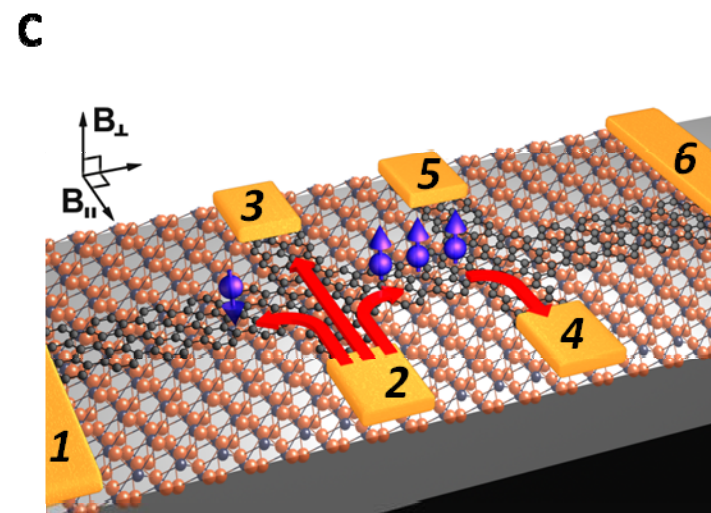
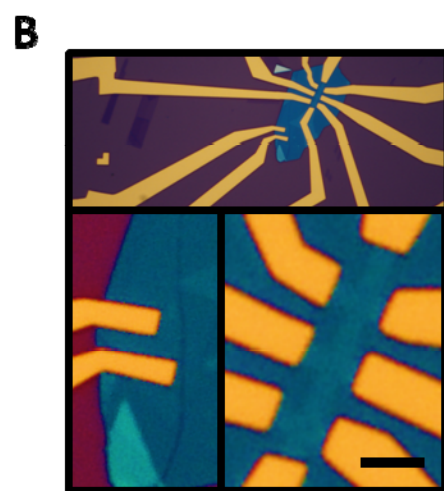
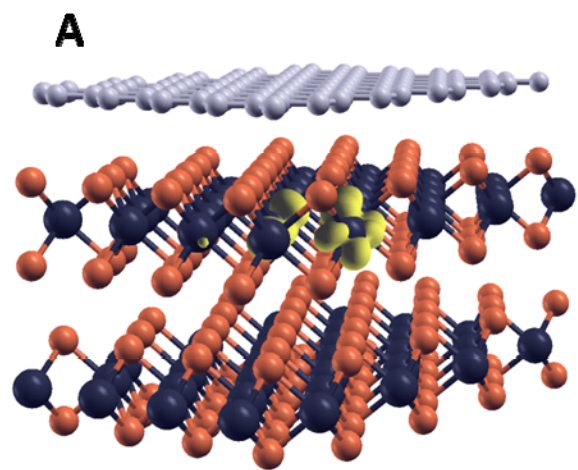
Fig. 2. Electronic transport measurement in graphene on WS₂ substrate: (A) Local resistivity (black lines) and conductivity (red line) measurement as a function of back gate voltage at 1.5 K. (B) Landau fan diagram of longitudinal resistance as a function of magnetic field and back gate voltage. (C) Corresponding plots of longitudinal resistance as a function of back gate voltage at constant magnetic fields. (Black and red lines represent 4.5 T and 12 T respectively.) Inset: Carrier concentration as a function of applied back gate voltage.

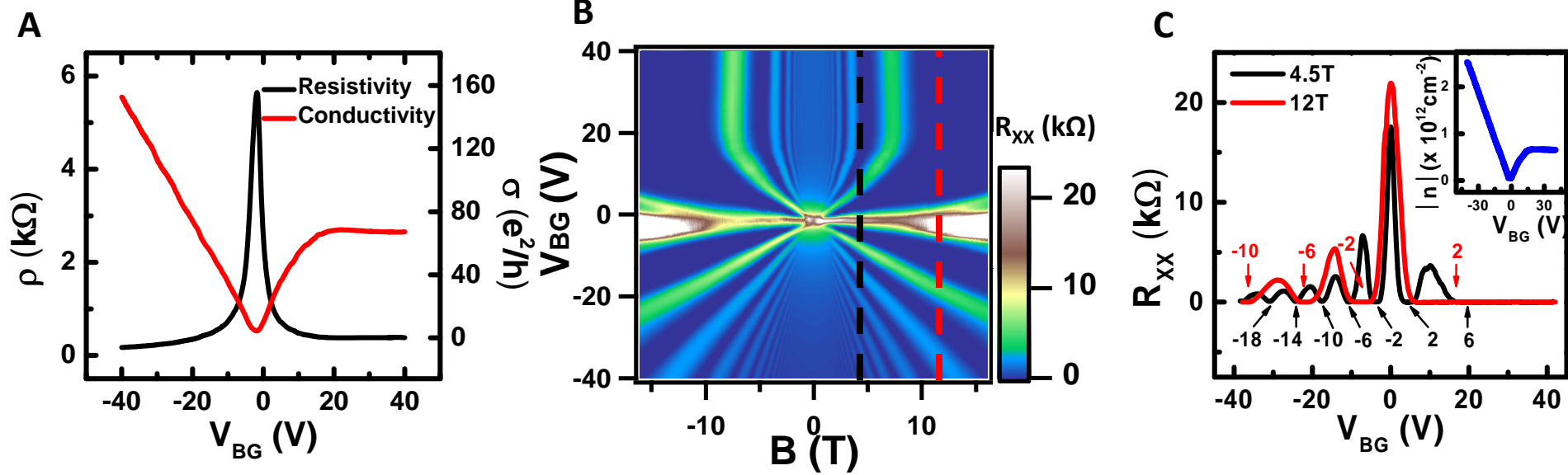
Fig. 3. Spin transport measurement in graphene on WS₂ substrate: (A) Nonlocal resistance measurement as a function of back gate voltage at RT in a reference graphene/SiO₂ device, Sample A, (red line) with its calculated Ohmic contribution (black line). (B-C) Nonlocal measurement for Sample B and Sample C at 1.5K and RT respectively. (Fig.3. B is the focused area of Inset Fig.3. B) (D) Fan diagram of nonlocal resistance as a function of in-plane magnetic field and back gate voltage. Color scale bar is adjusted to show between 12-20 Ω for clarification. Corresponding plots of non-local resistance as a function of in plane magnetic field at constant back gate voltages.(Black, pink and red lines represent 37 V , 2V (DP) and 37 V respectively.)

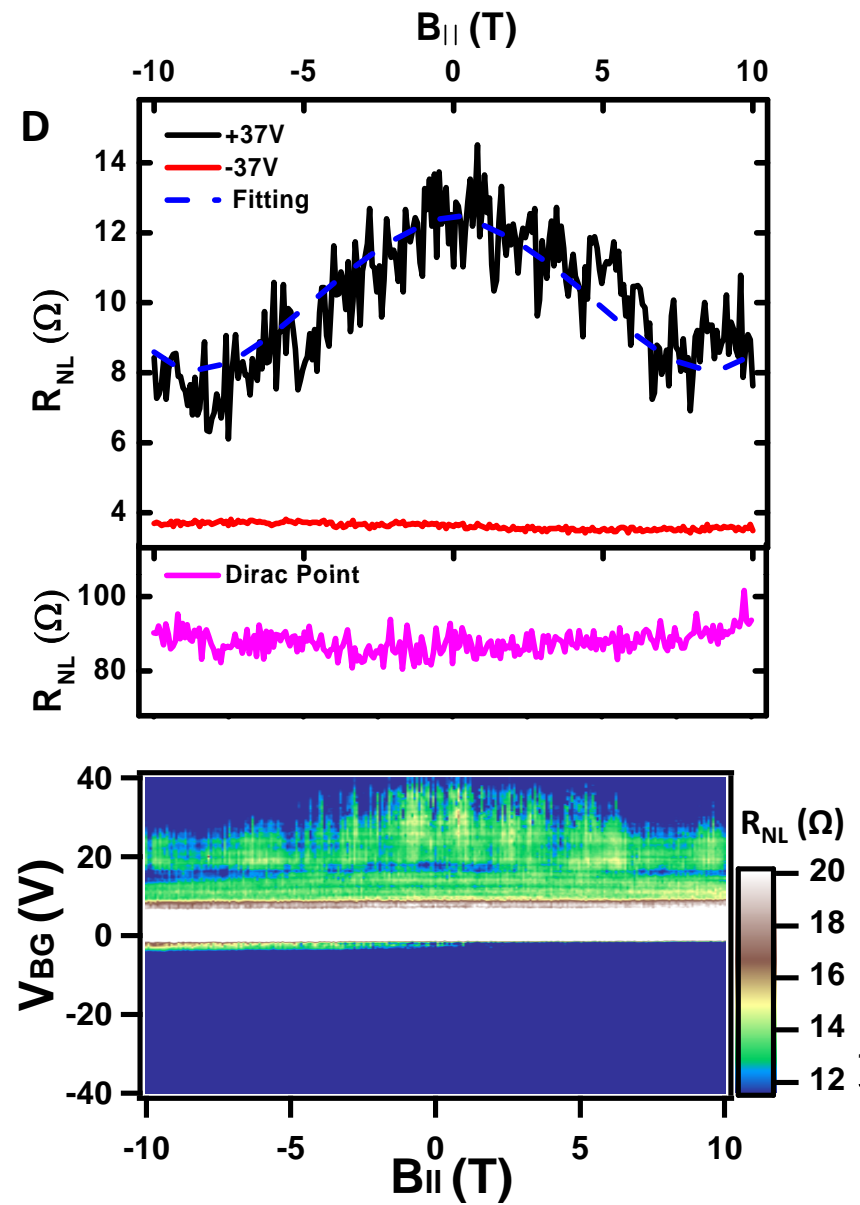
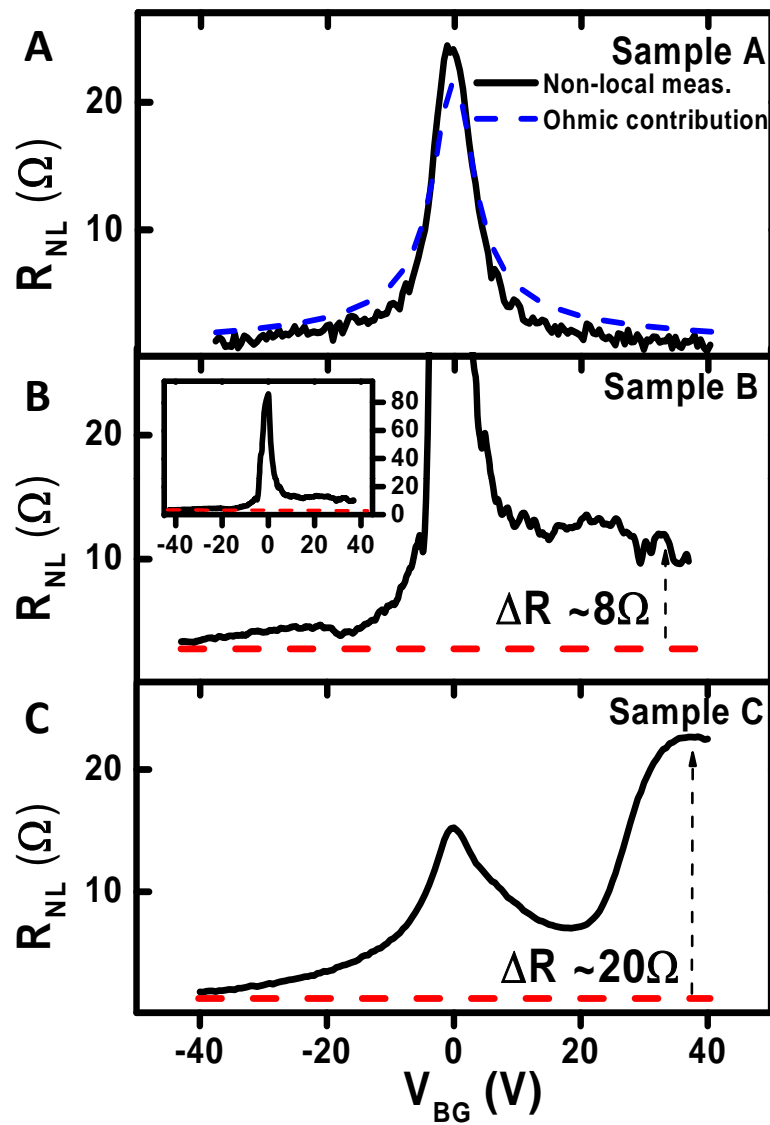
Fig. 4. XPS measurement of WS₂ and DFT bandstructure calculations: (A) High resolution XPS of W_{4f} and S_{2p} core levels. (B) Bandstructures for the interface between graphene and monolayer WS₂ and sulphur vacancy in bulk WS₂. Since the local or semi-local approximations for the exchange functional are known to result in an underestimation of the bandgap (our estimated value is 0.2eV smaller than the experimental value in ref. (30)), the unoccupied electron states in latter are shifted 0.2eV to correct the bandgap.

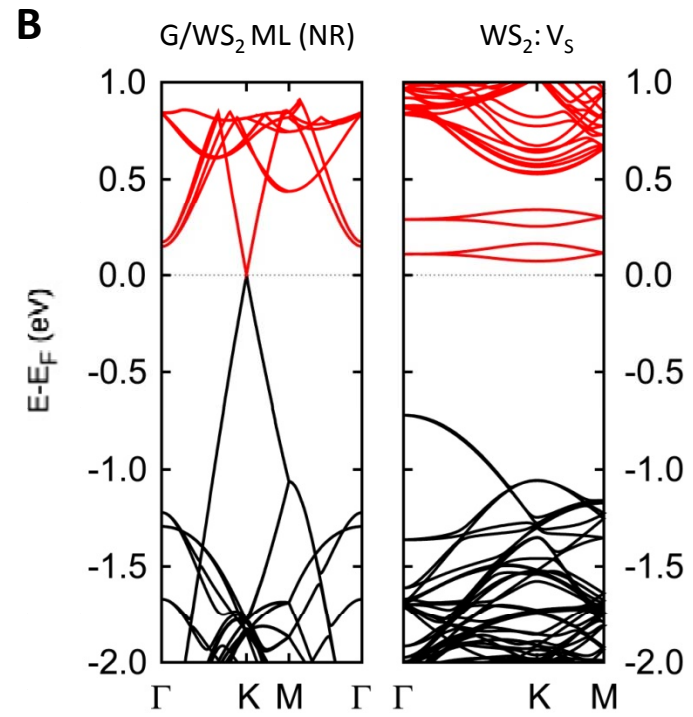
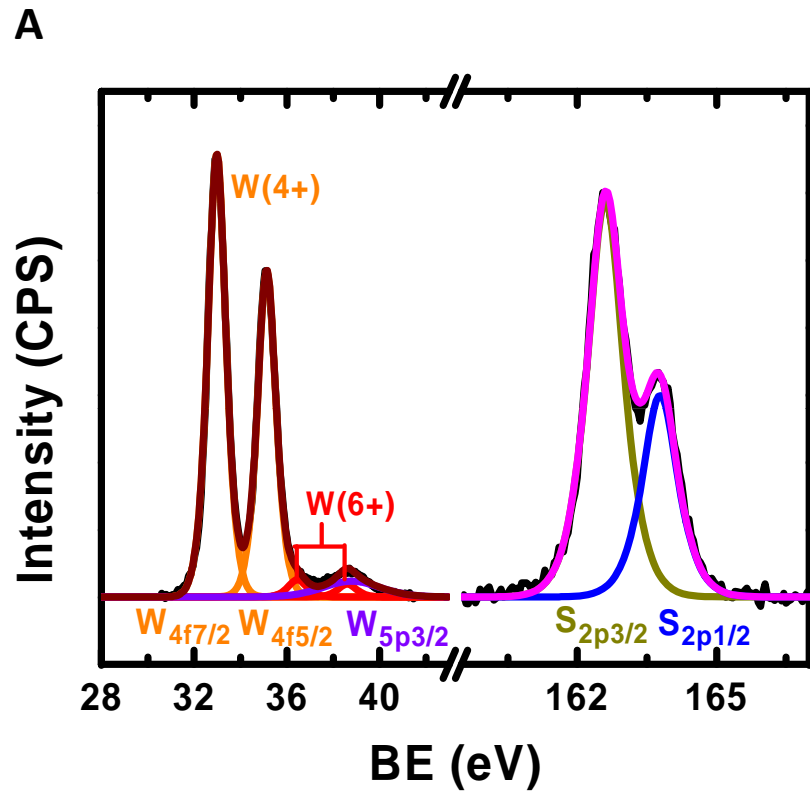
Figures

Spin-Orbit Proximity Effect in Graphene









Supplementary Materials for

Spin-Orbit Proximity Effect in Graphene

A. Avsar^{1,2}, J. Y. Tan^{1,2}, J. Balakrishnan^{1,2}, G. K. W. Koon^{1,2,3}, J. Lahiri^{1,2}, A. Carvalho^{1,2}, A. S. Rodin⁴, T. Taychatanapat^{1,2}, E. C. T. O'Farrell^{1,2}, G. Eda^{1,2}, A. H. Castro Neto^{1,2} & B. Özyilmaz^{1,2,3*}

¹Department of Physics, National University of Singapore, 117542, Singapore

²Graphene Research Center, National University of Singapore, 117542, Singapore

³NanoCore, National University of Singapore, 117576, Singapore

⁴Department of Physics, Boston University, Boston, MA, 02215, USA

*email: barbaros@nus.edu.sg

This PDF file includes:

Supplementary Text

Figs. S1 to S10

References

1. AFM and Raman characterization of WS₂ crystals

WS₂ flakes are prepared on SiO₂ substrates and then annealed in a gaseous mixture of Ar / H₂ (9/1) at 350°C for 3 hours to ensure the surface is free of residues. Figure S1a shows the typical optical and AFM images of few layers WS₂ with 12 nm thickness after the annealing process. The thickness of WS₂ substrates used in this study varied from 5 nm to 15 nm. Device B and Device C discussed in the main text have WS₂ thickness of 9 nm and 7 nm respectively. The surface topography shows that the surface roughness in WS₂ (~110 pm) is comparable to that of Boron Nitride¹.

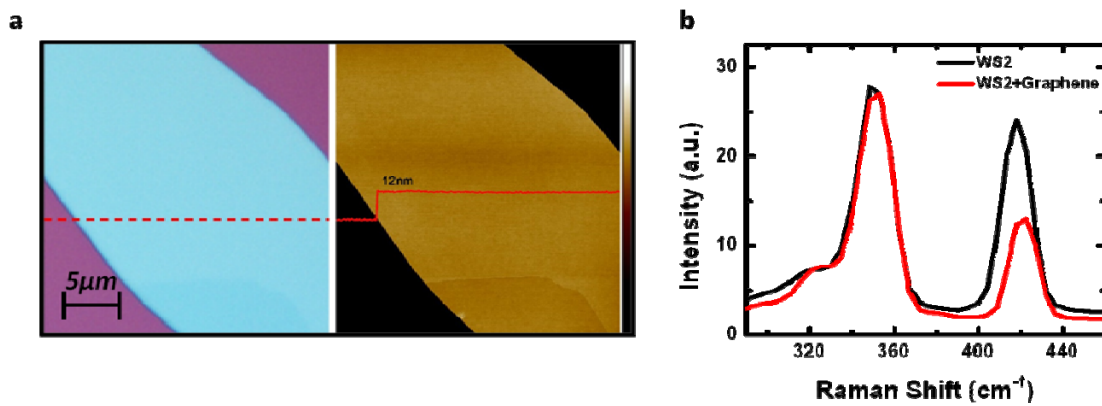


Figure S1. Crystal characterization. **a** - Optical and AFM images of a representative WS₂ flake. Color scale of the AFM image represents 0-20 nm. **b** - Raman spectrum of few layers WS₂ with and without graphene.

Figure S1b shows the typical Raman spectra of few layers WS₂ before and after graphene transfer. An excitation wavelength of 532 nm is used. The Raman spectrum is dominated by two peaks at 351 cm⁻¹ and 418 cm⁻¹ similar to those reported in reference 2. The peak at 351 cm⁻¹ is the overlapping of a first-order mode (E_{2g}¹ (Γ)) and second order mode that is activated by disorder (2LA (M)). The peak at 418 cm⁻¹ is due to another first order mode at the Brillouin zone, A_{1g} (Γ). Unlike the peak at 351 cm⁻¹, the intensity of the peak at 418 cm⁻¹ is reduced slightly after the graphene transfer. The laser power in this measurement is kept below 0.2mW to avoid any damage to the flakes.

2. Growth and XPS of WS₂ crystal

Bulk crystals of 2H-WS₂ were grown by the chemical vapor transport (CVT) method using iodine as the transport agent. As-received WS₂ powder (Alfa Aesar, 99.9 purity %) was sealed in an ampoule of fused quartz. The ampoule was kept in a temperature gradient from 875 to 935 C in a dual zone furnace for 1 week. WS₂ crystals grew on the cold end of the ampoule.

X-ray photoelectron spectroscopy (XPS) measurements were performed by using non monochromatic Mg *Ka* radiation (1253.6eV). Figure S2 shows the survey scan of a WS₂ crystal. Along with W and S core levels, O_{1s} and C_{1s} peaks are also observed. Next, we focus on the XPS spectra of W_{4f} and S_{2p} core levels (Fig. 4A). The W_{4f} core level peak can be fitted to two sets of doublets corresponding to W (+6) and W (4+) oxidation states. The presence of W (+6) oxidation states indicates that tungsten disulphide has undergone oxidation. The observed peak position for W_{4f7/2} for the +6 and +4 oxidations states matches with those reported in the literature³. The S_{2p} peak could be fitted to only one set of doublet corresponding to S-W bonding.

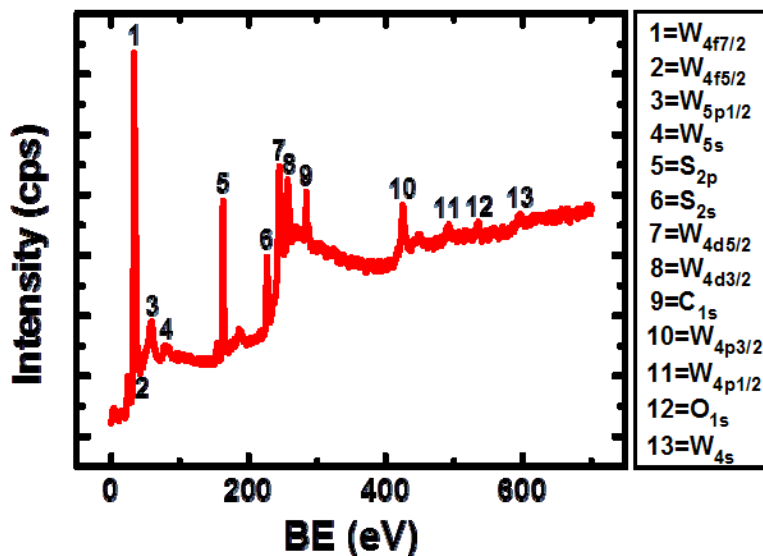


Figure S2. XPS survey scan of WS₂ crystal acquired with Mg *Ka* line.

The stoichiometry of WS₂ crystal was obtained from:

$$\frac{[W]}{[S]} = \frac{\sigma_{S2p}(h\nu)}{\sigma_{W4f}(h\nu)} \times \frac{\lambda_{S2p}}{\lambda_{W4f}} \times \frac{I_{W4f}}{I_{S2p}}$$

where $\sigma_{S2p}(h\nu)$ and $\sigma_{W4f}(h\nu)$ are photo-ionization cross sections of the 2p and 4f core level of sulphur and tungsten, respectively. The values of $\sigma_{S2p}(h\nu)$ and $\sigma_{W4f}(h\nu)$ are 0.045 and 0.18 Mb, respectively, obtained from tabulated data⁴. λ_{S2p} and λ_{W4f} are inelastic mean free paths (IMFP) of the photoelectrons with kinetic energies that correspond to the S and W core levels, respectively. The values of λ_{S2p} and λ_{W4f} were estimated to be 1.29 nm and 1.36 nm respectively using the Seah and Dench method⁵. I_{S2p} and I_{W4f} are the integrated intensities of the photoelectron peaks of the S_{2p} and W_{4f} levels after fitting, respectively. The error arising from the fitting is ~4%. With these values, the [W]/[S] ratio was estimated to be 0.57-/+0.02, which corresponds to 12 % sulphur vacancies in the crystal. Thus, the key findings of the XPS studies are that (1) the WS₂ crystals are notably sulphur deficient and (2) the sample is free of metal impurities in detectable concentrations. The origin of sulphur deficiency is partly due to the suspected partial oxidation and polycrystallinity of the sample. However, the estimate of 12 % is an upper limit to the sulphur vacancies for the following reasons:

First, our CVD-grown WS₂ crystal consists of 50~500 μm size polycrystalline grains, much smaller than the XPS probe size (~ 1 mm). The suspected presence of W terminated edge atoms (i.e. locally sub-stoichiometric) will lead undoubtedly to some errors in the estimation of the sulfur vacancies. It should also be noted that the surface terraces are expected to exhibit high concentration of edge defects. Therefore, in small scale atomically thin cleaved single crystal, WS₂ flakes used for our transport studies, the vacancy concentration is almost certainly smaller. The possible presence of divacancies is also like to further reduce this lower bound⁶.

With regards to oxidation, we observe a small fraction of W⁶⁺ states along with W⁴⁺ that are expected for ideal WS₂. Based on our fits, this amounts to approximately 4% of the total W atoms. It is conceivable that some of the sulfur vacancies are passivated by O atoms, or conversely, that some of the W signals are coming from WO₃ that may be present in the sample. In either case, this leads to a lower concentration of sulfur sites that are actually vacant, setting a lower bound to around 5 % (~1.2x 10¹⁴ cm⁻²).

Note also that W. Zhou et al.⁶ and H. Wiu et al.⁷ and have recently provided direct evidence that sulphur vacancies are abounded in CVT grown molybdenum disulfide. Since TMDCs have similar structures and properties, similar sulphur vacancy concentration in WS₂ is expected. Both results, ours based on XPS and theirs based on TEM imaging is in order of magnitude agreement for.

Based on all these considerations, we conclude even just assuming the lower bound it is reasonable there is a large concentration of sulphur vacancies of the order of 10^{13}cm^{-2} . This is significantly larger than the concentration of other impurities and thus the vacancies play a dominant role in the phenomenon that is reported in this study.

3. First-principle calculations

Our XPS measurements clearly indicate that WS₂ crystals have oxygen impurities and sulphur deficiency. To check the effect of such defects we have performed non-relativistic DFT calculations by using the method described in reference 8. For the dispersion we used the correction by Grimme⁹. Bulk WS₂ was modelled using a $4\times 4 \times 1$ supercell, with the experimental c/a ratio. The graphene-WS₂ monolayer interface was modelled in a supercell with 3×3 primitive cells of WS₂ and 4×4 primitive cells of graphene, with the respective lattice vectors aligned.

We investigated Si and O replacing for S (noted Si_S and O_S), adsorbed oxygen (noted O_{ad}) and S and W vacancies. The substitutional configuration is shown in Fig. S3-a. The two configurations found by Ataca et al. [S10] are depicted in Fig. S3. b-c. The O_{ad} configuration II (Mo₁ in Ref. 10) is 1.7eV higher in energy than the O_{as} configuration I (S₄ in Ref. 10). Finally, the S and W vacancies are modelled by removing the respective atoms. In both cases there is little lattice reconstruction.

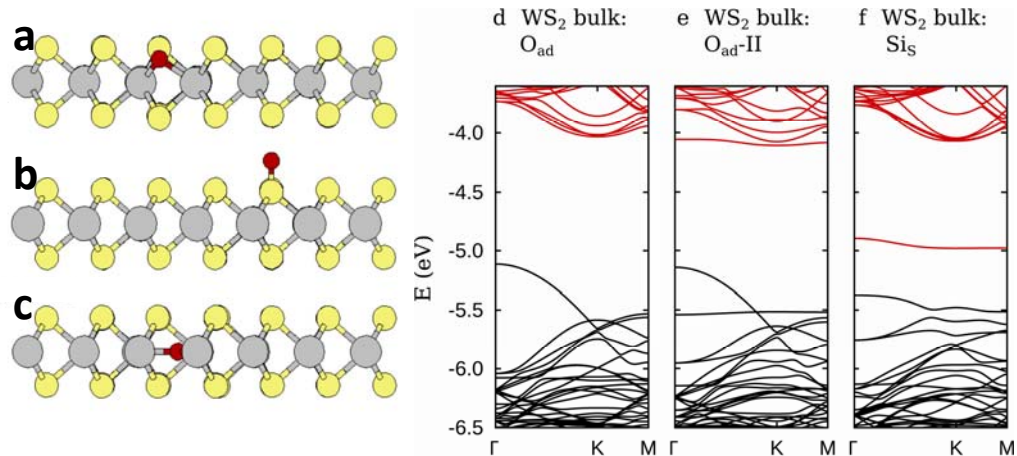


Figure S3. Geometry of a- O substituting for S b- adsorbed oxygen on the S layer c- adsorbed oxygen in the W layer. Bandstructures of defects in bulk WS₂: oxygen in the d,e - S₄ and Mo₁ positions, and f- substitutional silicon.

The non-relativistic bandstructure of bulk supercells containing defects with levels in the gap are shown in Fig. S3d-f. The position of the conduction band is underestimated by 0.2 eV within the working approximations. This underestimation is systematic and well known.

Stability

Since the only oxygen defect that is an electron acceptor is metastable, we investigated how likely it is to be present in the samples in that configuration. As the local bonding environment and even the bandstructure of the defects considered here are very similar in bulk and monolayer WS₂, we used a monolayer to model their stability:

1. Above the temperature of mobility of the sulphur vacancy: In thermal equilibrium, the stability of a substitutional atom X_S versus an adsorbed atom of the same species X_{ad} can be characterized by the enthalpy change associated with the capture of the impurity atom a sulphur vacancy: V_S+X_{ad} > X_S where V_S is the sulphur vacancy and X_{ad} is the adatom. For oxygen, this reaction enthalpy is -3.5 eV and -5.2 eV in configurations I and II, respectively. For silicon, the reaction enthalpy is -2.8 eV. These values are larger than the formation energy of a sulphur vacancy in a S-poor material. Therefore, Si and O occupy predominantly substitutional positions.

2. Below the temperature of mobility of the sulphur vacancy: We also investigated the hypothesis that, at temperatures at which Vs is immobile, oxygen can be introduced into the metastable position II. The calculated activation energy for the transformation $O_{ad-I} \rightarrow O_{ad-II}$ is 4.3 eV in the forward direction. This energy barrier prevents the introduction of O_{ad} into the II site below 590K.

4. Charge transport in few layer WS_2

In both local and non-local measurements in graphene on WS_2 substrate, a 100 nA a.c. current is used while the back gate voltage (V_{BG}) is swept from 40V to -40V. Devices are fabricated with Cr/Au contacts with thickness of 2 nm/ 100 nm.

It is well known that it is challenging to form Ohmic contacts to semiconducting 2D crystals¹¹⁻¹². In order to minimize the charge injection into WS_2 in our heterostructure devices, we deliberately look into a metal that exhibit large contact resistance. A recent study by McDonnell et al. reveals that Cr reacts with TMCS leading to formation of a highly defective and resistive interface¹³. Unlike Cr, Ti is reported not to react with MoS_2 . M. Fontane et al. also reported that MoS_2 is very strongly n-type dope if contacted with Cr/Au (2nm/100nm) such that no conduction is observed until $V_{BG} > 60V$ ¹⁴. We observe a similar behavior on WS_2 . Fig. S4 compares the transport characteristic of few layers of WS_2 contacted with Cr/Au (2 nm/100 nm) and Ti/Au (2nm /100nm) contacts. The WS_2 sample with Cr/Au shows an insulating response under a bias voltage of 0.1V with a gate sweep from 40V to -40V. On the other hand, the WS_2 sample fabricated with Ti/Au contacts shows a typical semiconducting behavior. Thus, we choose Cr/Au contacts for our graphene/ WS_2 heterostructure devices so that we make Ohmic contact to graphene but not to WS_2 directly. This minimizes the chance of having a small but finite, parallel conducting channel.

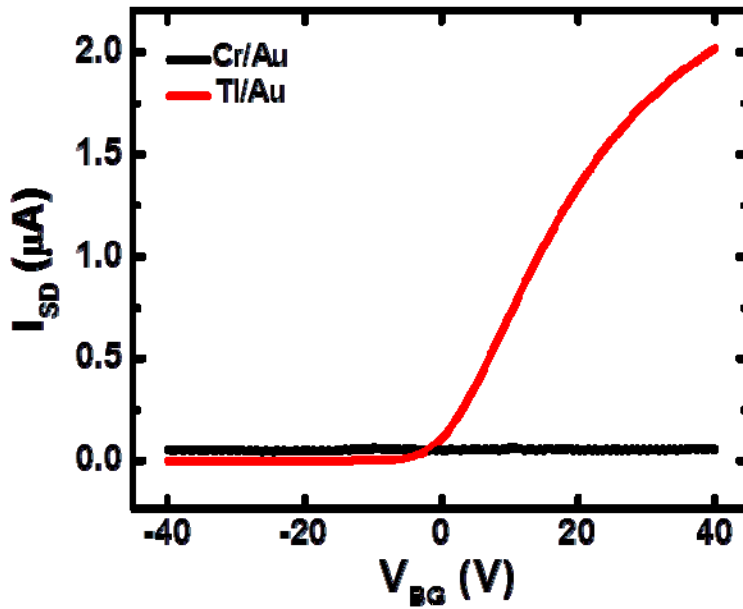


Figure S4. Two terminal resistance measurement in few layers of WS_2 flakes fabricated with Cr/Au and Ti/Au contacts. With Cr/Au contacts the source drain current remains negligibly small over the entire gate voltage range ($I_{SD} < 50$ nA).

5. Charge transport in Graphene/ WS_2 heterostructure

Figure S5 shows the resistivity and conductivity of graphene on WS_2 substrate (Sample D) as a function of V_{BG} at 6K. Also, for this sample the conductivity is linear in V_{BG} on hole side, but sample exhibits a V_{BG} independent conductivity above a threshold back gate voltage, ($V_{TH} \sim 15$ V). The sample has a field effect mobility of $\sim 50,000$ $cm^2/V.s$ at low densities is extracted using $\mu = \frac{I_{SD}}{C V_{BG} \Delta V}$, similarly to the reported values for graphene on BN substrates¹.

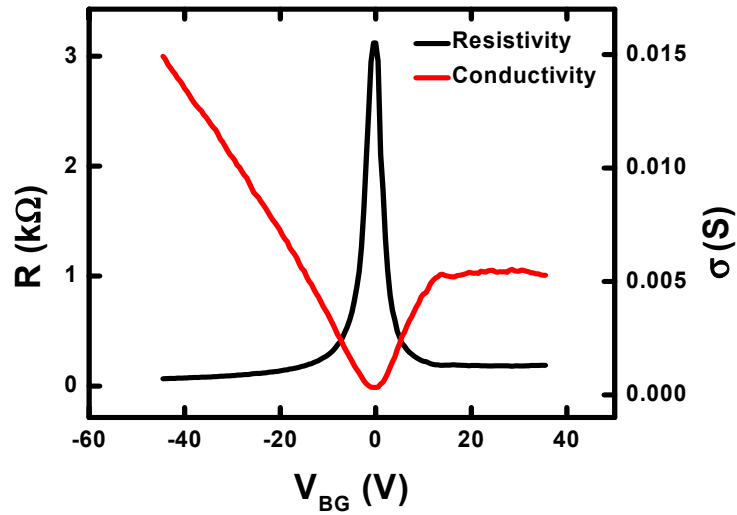


Figure S5. Resistivity and conductivity plots (black and red curves respectively) as a function of backgate voltage in graphene on WS₂ substrate at 6K.

6. Charge transport in inverse structure

As discussed in supplementary section #4, special attention is given to minimize the shunting of current through WS₂ during the transport measurements in heterostructure devices. In order to further rule out that the observed gate voltage dependent saturation in signal arises due to a gate voltage dependent conduction in WS₂, a top gated graphene/WS₂ heterostructure is fabricated by utilizing PVDF as dielectric. PVDF has been demonstrated to induce high charge carrier densities up to $3 \times 10^{13} \text{cm}^{-2}$ into graphene¹⁵.

Inset Fig.S6 shows the optical image of the top gated device. Thick PVDF dielectric (500nm) is spin coated to minimize the leakage current. Figure S6 shows the conductivity of graphene on WS₂ substrate as a function of top gate voltage (V_{TG}). Similarly back gated devices; we observe the saturation in conductivity at electron side. This observation demonstrates: 1-) The saturation in graphene conductivity is not due to parallel conductance of WS₂ as the charge carriers in graphene is tuned through PVDF dielectric rather than WS₂ itself. 2-) The persistence of saturation in graphene conductance even at high V_{TG} show that the density of sulphur vacancies to be at least in the order of 10^{13}cm^{-2} . This concentration of vacancies has an order of magnitude agreement with the sulphur vacancy concentration estimated from our XPS analysis.

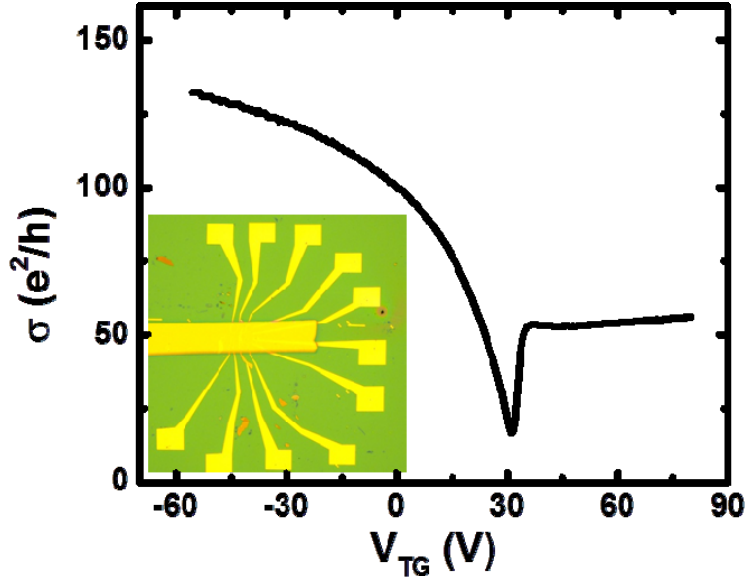


Figure S6. Conductivity of graphene as a function of top-gate voltage in “Top-gate/PVDF/Graphene/WS₂/SiO₂/Si” heterostructure at room temperature. The inset is the optical image of the measured device.

7. Quantum interference measurements in graphene/WS₂ heterostructure

In this section we show local magneto-conductance measurements in perpendicular field, which demonstrate weak-antilocalization, providing independent evidence for strong spin-orbit coupling in the graphene-WS₂ heterostructure.

Fig. S7a shows conductivity against V_{BG} of a graphene-WS₂ heterostructure as described in the main text, Fig S7b shows local conductivity against perpendicular magnetic field; at $V_{BG} < V_{TH}$ we observe positive magneto-conductance while at $V_{BG} > V_{TH}$ we observe negative magneto-conductance, as is characteristic of a crossover from weak localisation to weak antilocalization on reaching the conductivity saturation region.

In order to fit to the Maekawa-Fukuyama expression for weak-antilocalization we find it necessary to rescale the data¹⁶. By doing so we obtain for the spin-orbit field $H_{SO} = 0.02 \pm 0.02$ T at $V_{BG} = -29$ V, and $H_{SO} = 0.16 \pm 0.02$ T at $V_{BG} = 14$ V. These values are consistent with those obtained in, respectively, the conduction and valence band of WSe₂, which has extremely similar

electronic structure as WS_2 ¹⁷.

We therefore attribute this magneto conductance to quantum interference effects in the WS_2 substrate and suggest that the rescaling necessary to fit to the Maekawa-Fukuyama expression is due to the presence of the graphene channel, which dominates the conductivity. This effect is described in detail in a forthcoming article¹⁸.

With regard to the mechanism for proximity induced spin-orbit coupling described in the main text, these results show that applying a positive backgate voltage, and thereby raising graphene towards the weakly spin-orbit coupled conduction band of WS_2 , instead accesses states that have strong spin-orbit coupling which is characteristic of the valence band of WS_2 ¹⁹. We attribute these strongly spin-orbit coupled states within the band gap of WS_2 to sulphur vacancies consistent with density functional theory.

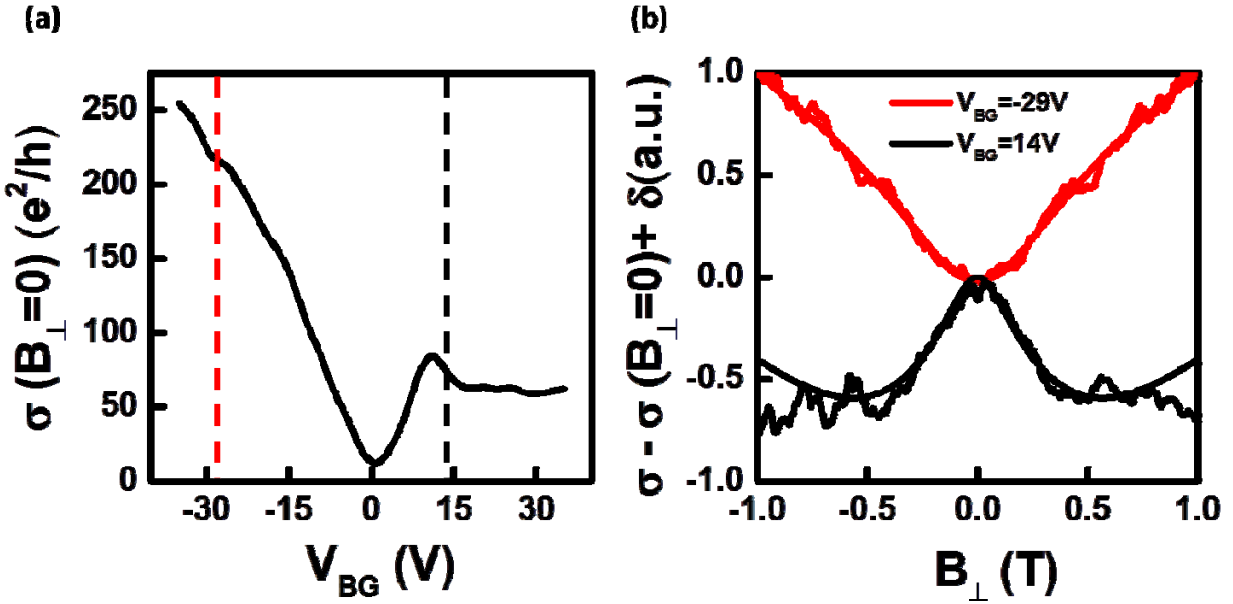


Figure S7: (a) Conductivity of graphene- WS_2 at zero magnetic field (b) Magneto-conductance of graphene- WS_2 measured at $T=1.2$ K in perpendicular magnetic field. The magneto conductance is rescaled and shifted to fit to the Maekawa-Fukuyama formula, the measurements show weak localization like behavior at negative backgate and weak antilocalization, associated with strong spin orbit splitting, at $V_{\text{BG}} > V_{\text{TH}}$. The black and red dashed lines in back gate voltage dependence of graphene conductivity plot shown in (a) represents the fixed back gate voltages where low field magnetic field dependent measurement was performed.

8. Magnetotransport measurements in high fields in Graphene/WS₂ heterostructure

As discussed in main text, electron carriers in graphene are populated into localized midgap states of WS₂ once the Fermi level aligns to these empty states. This leads to a graphene resistance that is independent of V_{BG} . In this section, we discuss the magnetic field (B_{\perp}) dependent resistance measurements in graphene/WS₂ heterostructure devices in more detail. Fig. S8a-b shows the longitudinal (R_{XX}) and Hall (R_{XY}) resistance of graphene as a function of V_{BG} at fixed perpendicular to the plane magnetic fields. The hole side shows regular integer quantum hall effect that is observed in high quality graphene devices. Uniquely to this system, on the electron side both R_{XX} and R_{XY} saturates above a $V_{TH} \sim 15V$. By tuning the Fermi level with B_{\perp} , it is possible to keep the Landau Levels completely filled over an extraordinarily broad range of back gate voltages. The observed phenomenon allows for sustaining a nondissipative current over a large back gate range, resulting in an unusual robust quantization of the resistance.

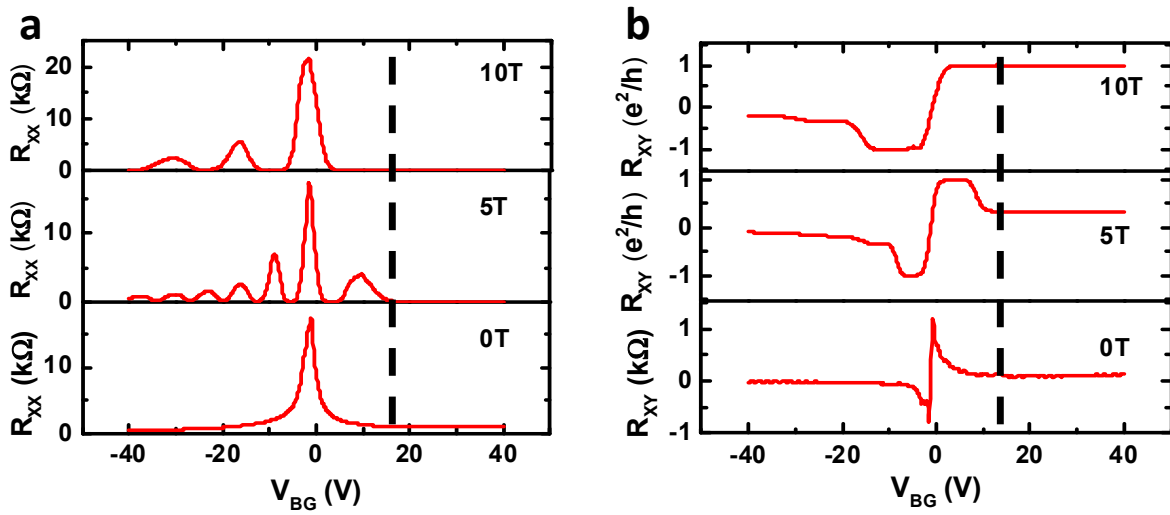


Figure S8. a,b - Longitudinal and Hall resistance measurements as a function of back gate voltage at fixed magnetic fields at $T = 1.5K$.

9. Effective mass calculation of graphene on WS₂ substrate

In this section, we determine the effective mass of charge carriers in graphene on WS₂ substrate by measuring the resistivity of sample B as a function of back gate voltage, perpendicularly applied magnetic field and temperature. Fig. S9a-b shows such Landau fan diagrams of the

longitudinal resistance at 15K and 30K. The amplitude of SdH oscillations is extracted from these color plots at fixed V_{BG} ranges with a step of $\Delta V=10$. Fig. S9c shows such plot at $V_{BG} = -20V$. The amplitude of SdH oscillations can be described by the following expression to extract effective mass of charge carriers:

where T is the temperature, m^* is the effective mass and h is the Planck constant²⁰. The gate dependence of m^* and carrier concentration is shown in Fig. S9d. While m^* increases slightly in V_{BG} on the hole side, similar to the previous report, it saturates above a threshold voltage on electron side²¹.

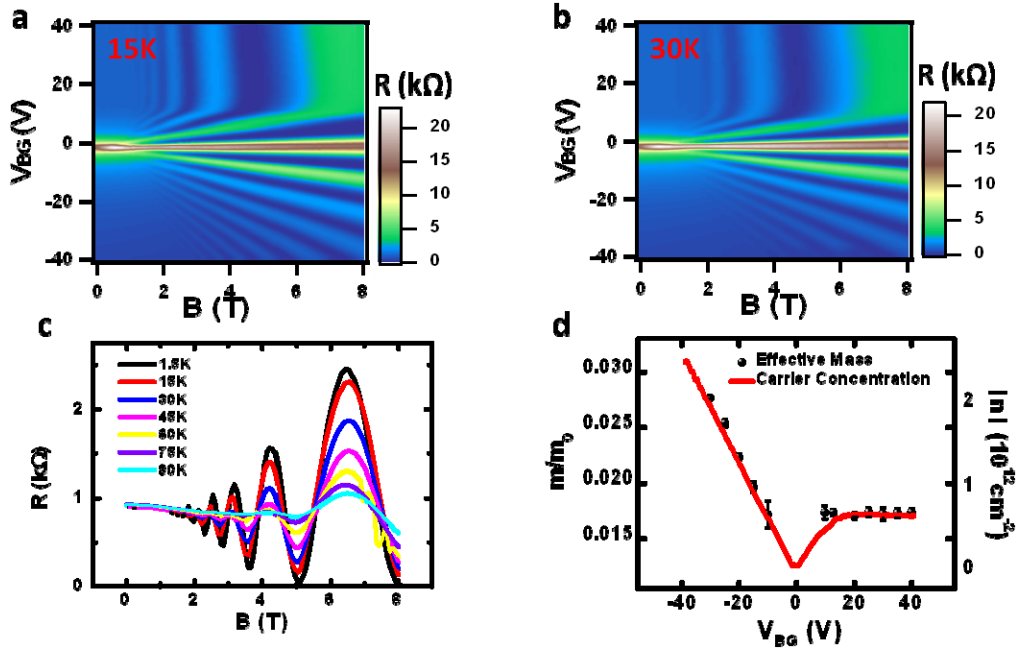


Figure S9. a,b - Landau fan plots of longitudinal resistance at 15K and 30K, c - Amplitude of SdH oscillation as a function magnetic field at different temperature values. d - Calculated effective mass and carrier concentration as a function of back gate voltage.

10. Additional non-local data

While the overall behavior of the non-local resistance as a function of V_{BG} is similar in all samples characterized, and shows a non-zero amplitude for most samples even on the hole side. However, as discussed in main text, the spin contribution to R_{NL} can be easily estimated in our devices, since the observed proximity effect exhibits a strong electron hole asymmetry. As expected, in samples with higher mobility this non-spin based background signal is much reduced. An example for such a device with a comparatively highly charge mobility ($\mu \sim 40,000 \text{ cm}^2/\text{V.s}$) is shown Fig. S10. Here the black line represents are fits of the Ohmic contribution. For $V_{BG} < V_{TH}$ the non-local signal is fully accounted for by the later. For $V_{BG} > V_{TH}$ we again see a strong enhancement of the non-local signal. We attribute the fluctuations in the non-local signal near the Dirac Point to the presence of charge puddles²².

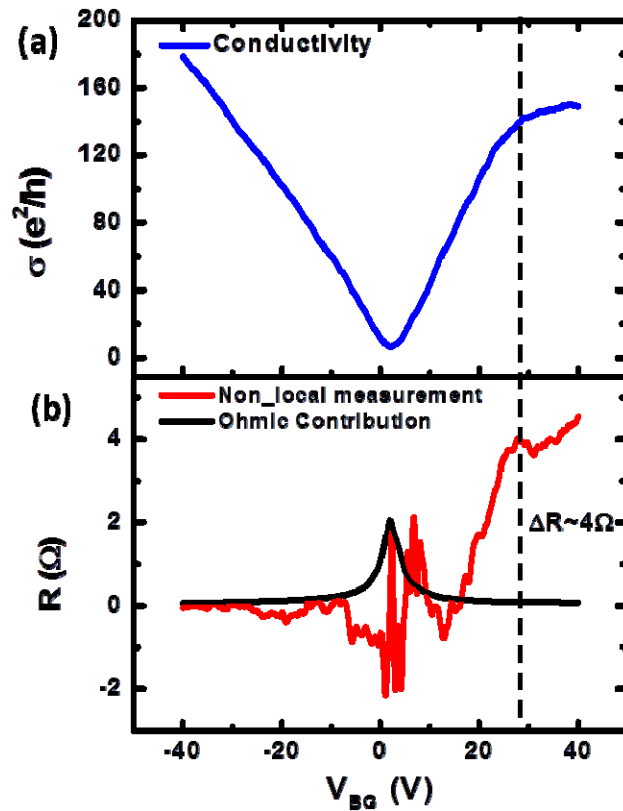


Figure S10. a,b - Local conductivity and non-local resistance measurement of graphene on WS_2 substrate. Black curve in b - represents the Ohmic contribution to the non-local signal. V_{TH} for this sample is at 29V.

REFERENCES:

1. C. R. Dean *et al.*, *Nature Nanotechnol.* **5**, 722–726 (2010).
2. A. Berkdemir *et al.*, *Scientific Reports*, **3**, 1755 (2013).
3. <http://ulisse.elettra.trieste.it/services/elements/WebElements.html>
4. F. Y. Xie *et al.*, *Journal of Electron Spectroscopy and Related Phenomena.* **185**, 112-118 (2012).
5. S. Tanuma, C. J. Powell, D. R. Penn, *Surface Science Lett.*, **192**, 849-857 (1987).
6. W. Zhou *et al.*, *Nano Lett.*, **13**, 2615 (2013).
7. H. Qiu *et al.*, *Nature Comm.*, **4**, 2642 (2013).
8. A. Carvalho, R. M. Ribeiro, Castro Neto, *Phys. Rev. B* **88**, 115205 (2013).
9. S. Grimme, *J. Comput. Chem.* **27**, 1787-1799 (2006).
10. C. Ataca, S. Ciraci, *J. Phys. Chem. C.*, **115**, 13303-13311 (2011).
11. I. Popov, *et al.*, *Phys. Rev. Lett.*, **108**, 156802 (2012).
12. S. Das, *Nano Lett.*, **13**, 100 (2013).
13. S. McDonnell *et al.*, *ACS Nano*, DOI 16.1021/nn5000449 (2014).
14. M. Fontana *et al.*, *Scientific Reports*, **3**, 1634 (2013).
15. Y. Zheng *et al.*, *Phys. Rev. Lett.*, **105**, 166602 (2010).
16. S. Maekawa, and H. Fukuyama, *J. Phys. Soc. Jpn.*, **50**, 2516 (1981).
17. H. Yuan *et al.*, *Nature Phys.*, **9**, 563 (2013).
18. E.C.T. O' Farrell *et al.*, to be submitted.
19. Z. Y. Zhu *et al.*, *Phys. Rev. B*, **84**, 153402 (2011).
20. K. S Novoselov *et al.*, *Nature*, **438**,197-200 (2005).
21. Y. Zhang, Y.-W. Tan, H. L. Stormer, P. Kim, *Nature*, **438**, 201-204 (2005).
22. J. Martin *et al.*, *Nature Phys.* **4**, 144-148 (2008).
23. D. A. Abanin *et al.*, *Phys. Rev. B*, **79**, 035304 (2009).